Shap. Mem. Superelasticity (2024) 10:45–54
https://doi.org/10.1007/s40830-023-00472-8

ORIGINAL RESEARCH ARTICLE

Effect of Post-treatments on the Thermomechanical Behavior of NiTiHf High-Temperature Shape Memory Alloy Fabricated with Laser Powder Bed Fusion

Timothée Cullaz[1,2] · Mohammadreza Nematollahi[1] · Keyvan Safaei[1] · Luc Saint-Sulpice[2] · Laurent Pino[2] · Saeedeh Vanaei[1] · Parastoo Jamshidi[3] · Moataz Attallah[3] · Othmane Benafan[4] · Shabnam Arbab Chirani[2] · Mohammad Elahinia[1]

Received: 1 September 2023 / Revised: 16 November 2023 / Accepted: 17 November 2023 / Published online: 28 December 2023

Abstract Despite increasing interest in Nickel Titanium-based high-temperature shape memory alloys (HTSMAs), machining challenges and limited functionality at elevated temperatures hinder their application in aerospace, energy, and automotive industries. Additive manufacturing, including laser powder bed fusion (LPBF) and subsequent treatments, addresses these obstacles. Employing LPBF, we processed a $Ni_{50.4}TiHf_{20}$ HTSMA, maintaining a constant volume energy density of 64 J/mm^3. Laser powers of 100 W and 200 W, with scanning speeds of 400 mm/s and 800 mm/s, respectively, were chosen for dense, defect-minimized parts. Process parameter effects on thermomechanical properties were assessed. Post-processing steps (HIP, solution treatment, aging) further enhanced properties. HIP proved more effective for 200 W samples. (Ti/Hf)-rich oxide inclusions formed during processing, impacting phase transformation temperatures. Aging treatments improved strain recovery, attributed to H-phase precipitate strengthening. After heat treatment, 100 W and 200 W samples exhibited 2.33% and 2.10% actuation strain, with negligible and near-zero residual strains.

✉ Timothée Cullaz
timothee.cullaz@rockets.utoledo.edu

[1] Mechanical Industrial and Manufacturing Engineering, University of Toledo, Toledo, USA

[2] UMR CNRS 6027, ENI Brest, IRDL, Brest, France

[3] School of Metallurgy and Materials, University of Birmingham, Birmingham, UK

[4] Materials and Structures Division, NASA Glenn Research Center, Cleveland, OH 44135, USA

Keywords Additive manufacturing · Hot isostatic pressing · Heat treatment · NiTiHf Materials · High temperature · Shape memory alloy

Introduction

NiTi is a widely employed shape memory alloy (SMA) in diverse applications, including aerospace, automotive, and energy industries, owing to its exceptional properties as well as unique characteristics of superelasticity and shape memory effect [1, 2]. However, its practical application is constrained by the limited martensitic transformation range (Ms below 100 °C), necessitating the development of new alloys suitable for elevated temperature applications. Introducing a third or fourth element into the binary NiTi SMA has been proven effective in engineering the transformation temperatures (TTs), allowing for control of the TTs within a wide range from subzero temperatures up to 1000 °C [3], depending on the type and quantity of the added element. Notable elements used for producing high-temperature SMAs (HTSMAs) include Pt, Pd, Zr, Hf, and Au [1, 2]. Among these alloys, NiTiHf and NiTiZr have garnered significant attention due to considerations of cost, weight, and thermomechanical behavior [1, 2]. By adding Hf in concentrations above—8%, the TTs of $NiTiHf_{20}$ (at.%) can be elevated up to 400 °C. Additionally, NiTiHf exhibits moderate ductility and remarkable dimensional stability, presenting further advantages [2]. These improved mechanical properties are attributed to the formation of H-phase precipitates after appropriate aging of Ni-rich NiTiHf.

The machining and manufacturing of NiTi-based alloys using conventional processes pose considerable challenges. A study revealed that the machining of NiTiHf alloy led to severe and uncontrollable tool wear, especially at high

cutting speeds [4]. Consequently, alternative techniques such as laser machining, Electro Discharge Machining (EDM), and Additive Manufacturing (AM) have gained significant interest in working with NiTi-based alloys. AM also offers several advantages over traditional methods, enabling the production of complex parts with precise control over the microstructure and local phase transformation changes [1]. This capability to tailor the microstructure and transformation temperatures of the shape memory alloy parts is particularly intriguing for customizing properties based on specific applications [1, 5].

Most of the current research in this area focuses on the laser powder bed fusion (LPBF) process for NiTi shape memory alloys [6, 7]. Through optimization of LPBF process parameters (PPs), dense NiTi parts with high density (above 98%) and mechanical performance comparable to or even superior to conventionally fabricated NiTi alloys have been reported in the literature [8–15]. However, the application of AM for high-temperature shape memory alloys (HTSMAs) remains relatively limited. Some studies have addressed the processability of Co–Ni-Ga HTSMA using LPBF [16–18], and there have been a few investigations into LPBF of Ni-rich NiTiHf alloys [19–21]. However, processing these alloys via LPBF presents cracking, delamination, porosity, and elemental evaporation challenges. These phenomena have a significant impact on functional properties such as transformation temperatures and mechanical responses [19–21]. Therefore, it is interesting to tune the process parameters and use post-treatments to prevent defects, increase density, and enhance the mechanical behavior.

This study aimed to investigate the manufacturing of high-temperature shape memory alloys by laser powder bed fusion method and post-treatments, including heat treatment and HIP, were assessed. Two sets of parts were fabricated, maintaining the same energy density, hatch space, and layer thickness of 64 J/mm3, 130 µm, and 30 µm, respectively. Additionally, two sets of laser power-scan speeds were used: 100W—400 mm/s and 200W—800 mm/s. The effect of process parameters on the microstructure and thermomechanical behavior of the fabricated parts was investigated.

Material and Method

A $Ni_{50.4}Ti_{29.6}Hf_{20}$ (at.%) alloy was utilized to produce powder for this study. The initial ingot was generated using the vacuum induction skull melting method and subsequently cast into bars (Flowserve US Inc., heat designated as FS#9). These bars were then employed in the gas atomization process under an argon atmosphere to produce the powder (Electrode induction-melting gas atomization by TLS Technique GmbH, Bitterfeld, Germany). We note that the powder used in this study was recycled a few times due to the limited amount of available powder. However, after sieving (Elcan Industries, Tuckahoe, NY) the particle diameters at 50% in the cumulative distribution of the recycled powder and commercial powder are, respectively, 49.7 µm and 55.04 µm. In addition, a particle shape analysis was performed on the virgin powder and the recycled powder. The average sphericities were 0.96 and 0.94 for the virgin and recycled powder, respectively. Thus, the recycled powder can be considered equivalent to the virgin powder in terms of particle size distribution and shape, suitable for LPBF process.

To fabricate the test coupons, a 3D SYSTEMS ProX 200 LPBF metal printer equipped with a 300W Ytterbium fiber laser (wavelength: 1070 nm, spot size: 80 µm) was used. The machine was operated in a protective atmosphere of Ar gas to prevent oxidation.

Based on the findings of our previous study [21], two sets of process parameters (PPs) were selected for further investigation. These parameters have previously achieved dense parts (above 98% density) without major defects and the density can be increased by a specific post-treatment [21–24]. In the first set of coupons, a relatively low laser power with a low scan speed was employed (100 W, 400 mm/s). On the other hand, the second set of coupons was fabricated using higher laser power and scan speed (200 W, 800 mm/s). The layer thickness and the hatch spacing were set constant at 30 µm and 130 µm. Consequently, both sets of process parameters (PPs) in this study maintain a constant energy density (E_v) of 64 J/mm^3. The specific details of the process parameters are presented in Table 1.

Using these PPs, a dozen test coupons were fabricated with dimensions of $4 \times 4 \times 10$ mm^3. It was observed that the volumetric energy density plays a crucial role in determining material behavior. Accordingly, this study demonstrated that the optimal balance between achieving the highest density and the least decrease in transformation temperatures is attained at an energy density of 64 J/mm^3. However, it has been shown in [10] that even with a constant energy density, the laser power can significantly influence the properties.

The samples produced with these process parameters are referred to as "as-built" (AB) hereafter. One batch of samples was investigated without any post-processes, while two other batches underwent different post-processing treatments for further study.

Table 1 Process parameters (PP) used to fabricate the test coupons

Coupon	Laser power (W)	Scan speed (mm/s)	Hatch space (µm)	Thickness (µm)	Energy density (J/mm^3)
100W-AB	100	400	130	30	64
200W-AB	200	800	130	30	64

An EPSI HIPping vessel (Temse, Belgium) was utilized to conduct hot isostatic pressing (HIP) with a heating/cooling rate of 5 °C /min. The temperature was held at 1050 °C for 2 h at 150 MPa under Argon pressure. Additionally, precipitation can occur during the HIP process, contributing to specific material characteristics. The samples which followed this post-treatment were called "AB + HIP" or "HIP". To precisely control the precipitation and achieve the desired functionality in NiTiHf alloys, a carefully selected heat treatment procedure was employed, based on literature references [25–27]. This procedure involved a solutionizing heat treatment at 1050 °C for 5 h, followed by water quenching (WQ), and an aging heat treatment at 550 °C for 3 h, concluded by air cooling (AC).

The samples that underwent the AB-HIP process, followed by the solutionizing and aging heat treatments, will be referred to as "AB-HIP-HT" samples or "HT" samples hereafter. Figure 1 illustrates the post-processing steps involved in this study.

For each of the following characterization tests, the three different conditions (AB, AB-HIP, and AB-HIP-HT) were investigated. A Perkin-Elmer Differential scanning calorimetry (DSC) was used with a heating and cooling rate of 10 K/min under a nitrogen atmosphere to obtain phase transformation behavior and transformation temperatures based on ASTM F2063. The phase transformation temperatures were determined using a tangent method based on ASTM E3097.

Prior to microstructure observation, the samples were mechanically polished using a Buehler AutoMet 250 Grinder-Polisher. Optical microscopy (OM) was performed using a Keyence VHX 6000 microscope. An FEI Quanta 3D FEG equipped with an EDX detector was used for scanning electron microscopy (SEM) and EDS analysis. The Ni, Ti, and Hf contents were determined using inductively coupled plasma atomic emission spectroscopy (ICP-AES), and impurities (O, N, and C) were analyzed via the inert gas fusion technique and combustion for CS content per ASTM E1512 and E1447. These element analyses present a calibration error of 0.2%.

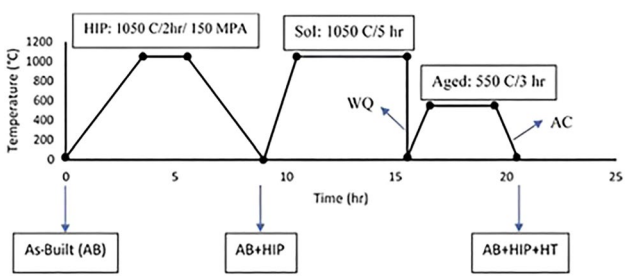

Fig. 1 Schematics of post-processing steps and terminology used throughout the document

Coupons were mechanically tested using an Instron Electromechanical compressive test bench with a 50 kN load capacity (model 5969, INSTRON). The strain was measured using a 12 M GOM system digital image correlation system (ENIB, IRDL, UME CRNS 6027), while temperatures were recorded through a K-type thermocouple. Constant load thermal cycling tests were performed, where samples were cycled between two temperatures. The temperature range was set below the martensite finish (Mf) and up to above the austenite finish (Af) of the specimen. During the thermal cycle, the specimens were loaded with a constant stress of 100 MPa. Subsequently, for each thermal cycle, the stress was increased by 200 MPa increments up to 700 MPa.

The methodology was developed per ASTM E3097 [26] to determine shape memory properties, such as transformation strains and actuation strains. The actuation strain was calculated as the difference in strain between the austenite start (As) and the Upper Cycle Temperature. The residual strain was determined by the strain observed after the thermal cycle was completed.

Results and Discussion

Composition, and Microstructure Analysis

The element composition analysis measured a slight drop (1%) in Nickel content when the laser used 200W for the fabrication, even with the constant energy input. Laser power plays a role in Ni evaporation causing Ni loss even at identical energy density [10]. This can be explained with respect to the fact that Nickel boiling temperature and vapor pressure are lower compared to Hafnium and Titanium [10, 28]. Thus, high laser powers result in high-temperature melt pools and vaporization, which is consistent with the literature [19, 29]. Also, the analysis revealed Oxygen pickup in both conditions 617 ppm and 543 ppm for 100W-AB and 200W-AB samples, respectively. The impact of oxides in the matrix will be discussed later in the manuscript.

Porosity levels of additively manufactured parts were investigated using optical microscopy. The porosity level is determined by the fraction of the porosity area relative to the total measured area. Three observations are carried out for each sample and the average values are shown in Table 2. Figure 2 shows the main defects that we found in the optical micrographs. In the case of 100W samples, relatively higher porosities can be observed in comparison to the 200W samples. The highest porosity level is 1.27% reported in the 100W-AB sample due to the presence of lack-of-fusion defects attributed to the insufficient melt pool width which proved to be challenging to remove even with the optimized process parameters [21] (Fig. 2a). On the other hand, the 200W-AB sample shows a lower density of pores (Fig. 2d).

Table 2 Porosity calculated based on the area of the pores over the total measured area for 3 different sample conditions

PPs	100W	200W	100W	200W	100W	200W
Condition	AB	AB	AB + HIP	AB + HIP	AB + HIP + HT	AB + HIP + HT
Porosity level (%)	1.27	0.11	0.57	0.07	0.57	0.28

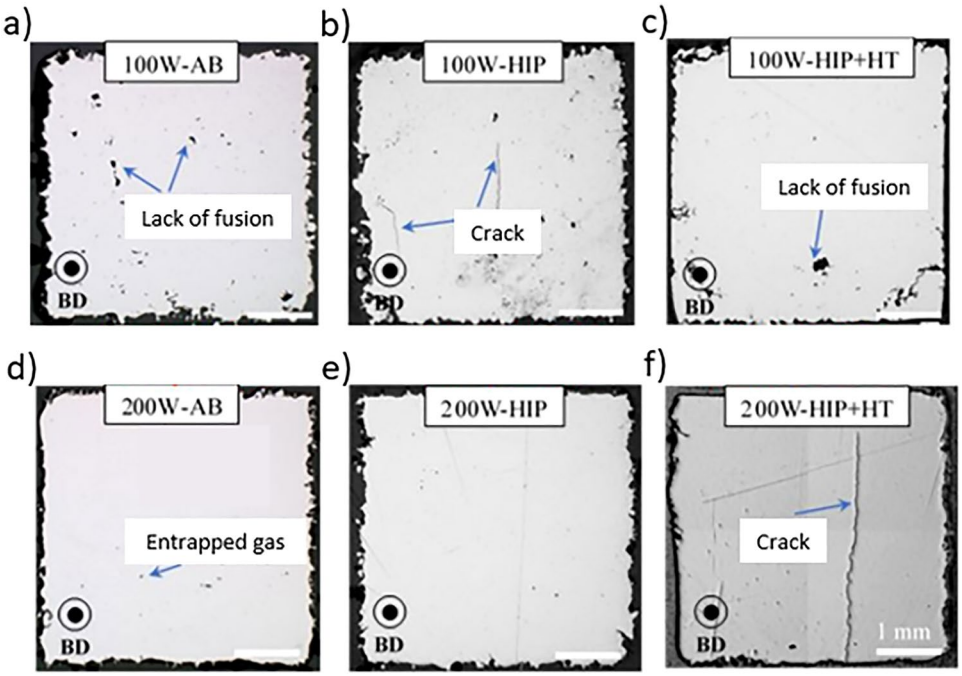

Fig. 2 Optical micrographs of the samples in different conditions which show the main structural features. (**a**) 100W-AB sample, (**b**) 100W-HIP sample, (**c**) 100W-HIP + HT sample, (**d**) 200W-AB sample, (**e**) 200W-HIP sample, and (**f**) 200W-HIP + HT sample

In both cases (100W and 200W samples), HIP was used to increase the density through closing pores. Nevertheless, the selected parameter used for the HIP can be optimized as some internal defects are still present in the sample (Fig. 2b, 2e). However, with the heat treatment, if the porosity level is not zero, the heat can drive gas expansion and increase the porosity level from 0.07% to 0.28% in the 200W condition (Fig. 2c, f). This mechanism has been highlighted previously [30, 31]. Some microcracks were observed in coupons 100W-AB + HIP and 200W-HIP + HT. Due to the presence of some cracks after HIP, the porosity may be connected to the surface. Thus, during heat treatment, the gas is not entrapped and won't lead to an increase in the porosity level. In addition, due to the low number of pictures to measure the porosity level the observed cracks can induce some uncertainty. Parallely, micro-CT scan analysis will be performed in future works to complete this analysis and allow us to characterize the defects more precisely.

Figure 3 shows SEM micrographs of selected samples after HIP and heat treatment. In general, all the samples regardless of their condition showed two types of inclusions: non-metallic and intermetallic in the form of fine oxide throughout the matrix. Arrows show inclusions revealed in the backscatter SEM micrographs and two different inclusions were distinguished with black and white colors (Fig. 3a–f). EDS analysis revealed that white regions are rich in Oxygen, Hafnium, and lean in Nickel, and Titanium and are most likely HfO_2 inclusions (Fig. 3g). Therefore, based on EDS the black inclusions are enriched in Titanium and Oxygen, which are typically formed as $(Ti + Hf)_4Ni_2O_x$. Both inclusions were reported previously for the NiTiHf alloys [26, 32]. These oxides are formed due to the high levels of oxygen in the used powder and during the fabrication. Their roles are described in the following sections.

Phase Transformation Behavior

Figure 4 shows the transformation temperatures including austenite start (As), austenite finish (Af), martensite start (Ms), and martensite finish (Mf), for NiTiHf powder and two sets of PPs including as-built and post-treated conditions. Table 3 summarizes martensite start (Ms) and austenite finish (Af) for the different sample conditions.

Starting with the as-built conditions, both samples showed single and broadened transformation peaks. Local composition inhomogeneity, the existence of dislocation, inclusion/precipitate formation, and residual stress resulting from the process can lead to the peak broadening of the as-built samples [33–35]. The transformation temperatures of 100W-AB and 200W-AB are greater than 60 °C and 70 °C

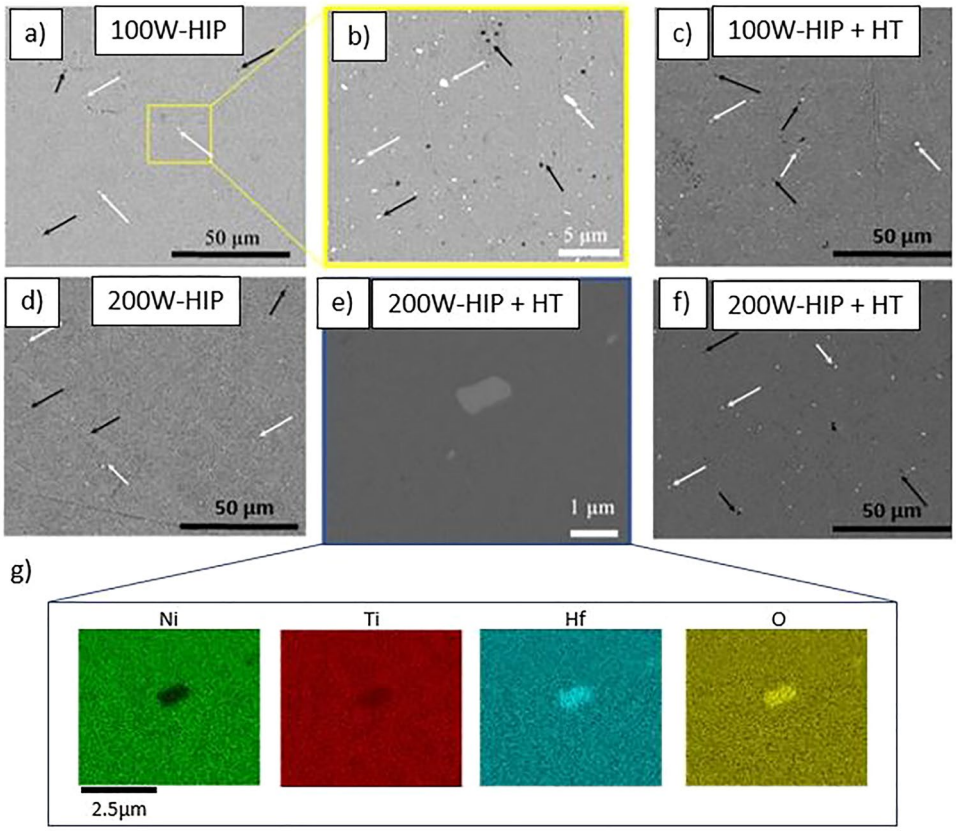

Fig. 3 SEM images and EDS analysis for different sample conditions. (**a**) 100W-HIP, (**b**) zoom in of the image (**a**, **c**) 100W-HIP + HT sample, (**d**) 200W-HIP sample, (**e**) 200W-HIP + HT sample, (**f**) 200W-HIP + HT, (**g**) EDM maps of Ni, Ti, Hf and O elements of the image (**e**)

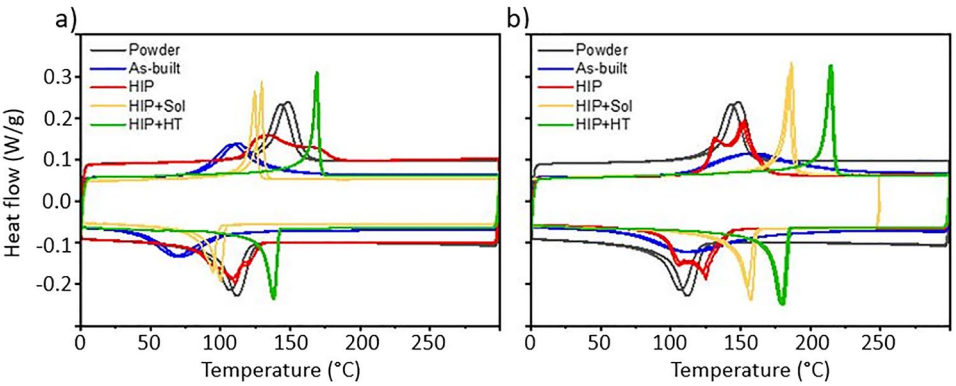

Fig. 4 DSC graphs of (**a**) 100W and (**b**) 200 W including as-built, HIP, solution treatment, and aged conditions

Table 3 Transformation temperatures reported from the DSC results

Power	Samples	Ms (°C)	Af (°C)
100W	AB	100	125
100W	HIP	130	180
100W	HIP-HT	142	170
200W	AB	160	200
200W	HIP	140	170
200W	HIP-HT	180	220

different for Ms and Af. The main transformation temperature alteration in NiTiHf alloys derives from the compositional changes of the matrix (i.e., Ni [at.%] /(Ti + Hf) [at.%] ratio), which is mainly affected by the process parameters in the LPBF process. Compositional changes that occurred in the LPBF may be attributed to Ni loss and the formation of precipitates/inclusions [13, 19–22]. It is confirmed by the results obtained from Inductive Coupled Plasma (ICP), which showed a lower Ni content of 200W-AB sample than

100W-AB and can explain the higher TTs of 200W-AB. Here, despite the same volume energy density of both samples, a higher Ni loss is expected in the 200W-AB sample in comparison with 100W-AB. But it has been shown that laser power plays an eminent role in Ni evaporation and transformation temperature modification, and it is consistent with the literature [10, 35].

In addition, the decreasing trend in the transformation temperatures of 100W-AB sample with respect to the powder can be primarily attributed to the existence of Ti/Hf-rich oxide inclusions, i.e. HfO2 and $(Ti+Hf)_4Ni_2O_x$, as shown in the microscopy section. The formation of such inclusions lowers the transformation temperatures by depleting Ti/Hf and increasing the Ni/Ti ratio in the matrix, consequently [32]. Depending on the process parameters both mechanisms may happen in the process: the Ni loss and the Ti/Hf-rich inclusion formation. The final transformation temperatures are controlled by the trade-off between these two mechanisms. However, due to the interaction between both mechanisms, it is not possible to precisely quantify the Ni loss according to the laser power.

At first glance, the follow-up heat treatments, HIP, solutionizing, and aging, clearly have altered phase transformation behavior. Multi-stage transformation peaks during forward and reverse transformation can be found for both samples after the HIP process. Therefore, two competing effects contribute to the phase transformation behavior of the alloy: the Ni depletion in the matrix due to the H-phase precipitation and the reinforcement effect of coherent H-phase [35–38]. The first effect causes an increase and the second mechanism results in a drop in transformation temperatures. Short-time and low-temperature aging process may lead to the formation of a fine H-phase with a low volume fraction and transformation temperature drop. In addition, the effect of Ni depletion becomes more considerable with increasing time and temperature. Thus, the decrease in transformation temperatures of 200W-AB + HIP sample after HIP may confirm that the reinforcement effect of the fine H-phase precipitates is the primary result of the transformation temperature alternation. It has been shown in [36] that the NiTiHf with higher Ni content is more sensitive to transformation temperature increase along a heat treatment due to the loss of Ni in the matrix during the H-phase precipitation. Then, the 100W-AB + HIP sample presents a higher Ni content than the 200W-AB + HIP due to a lower laser power during the fabrication therefore the transformation temperatures increase.

After follow-up solution and aging heat treatments single and narrow DSC peaks with good thermal stability were achieved in both conditions. The formation of the fine, coherent, and uniformly dispersed H-phase precipitates after aging results in material strengthening and stable phase transformation [33, 35]. The Ni depletion due to the formation of the oxides can explain the increasing trend of the transformation temperatures after aging.

Thermomechanical Behavior

Compressive constant force thermal cycling responses of selected alloys are presented in Fig. 5. As the stress level increases transformation temperatures tend to be higher, a typical stress effect on phase transformation behavior.

The actuation and residual strain are shown in Fig. 6 based on the standard measurement presented in the method section. The actuation strain gives the material potential for the material to deform during a thermal cycle under constant stress. The larger the actuation strain, the bigger the potential to answer actuator challenges. However, actuation systems require stability in the behavior [37]. Thus, during thermal loading, the residual strain that can appear needs to remain as low as possible. In Fig. 6, the actuation strain increases when higher stress is applied. At low stress, mainly self-accommodated martensite plates could be formed. But, when the stress increases the activation of the martensite variants in the direction of the loading appears and observes a larger actuation strain [23, 38]. The 100W-AB and 200W-AB samples showed an increase of 0.38% and 0.35%, respectively, between the 100 to 700 MPa. Parallelly, the residual stress increases with the applied stress due to plastic deformation which can occur during the reverse transformation when some martensite variants fail to transform back into austenite due to lattice defect or dislocation which can be present in as-built configuration [2, 23, 37, 39].

After HIP process, in both sample sets (100W and 200W), actuation strains increased. At 500 MPa, 100W-AB + HIP sample showed 2.51% actuation strain with 0.18% residual strain, while 200W-AB + HIP exhibited 2.38% actuation strain with 0.55% residual strain. Increasing the stress level to 700 MPa, resulted in a drastic change in the residual strain in the 200W sample (1.4% of residual strain with 1.74% actuation train). The literature explains that HIP allows dislocation annihilation, and grain coarsening, which enhances the actuation strain [23], additional work needs to be carried out to observe these phenomena. Therefore, the increase in actuation strains can be due to the formation of H-phases during the slow cooling of HIP process as outlined in Sect. 3.3. A good coherency and continuity of the austenite phase and H-phase grains interface has been shown in the literature for NiTiHf alloys when the H-phase grains are smaller than 20 nm. However, this coherency is lost when the austenite and H-phase matrix is transformed to martensite [35, 40]. In the case of larger H-phase grains, accommodation would not happen due to the transformation strain around a large particle and become obstacles for further martensite plate growth. While in the case of small precipitates, the strain due to the mismatch between

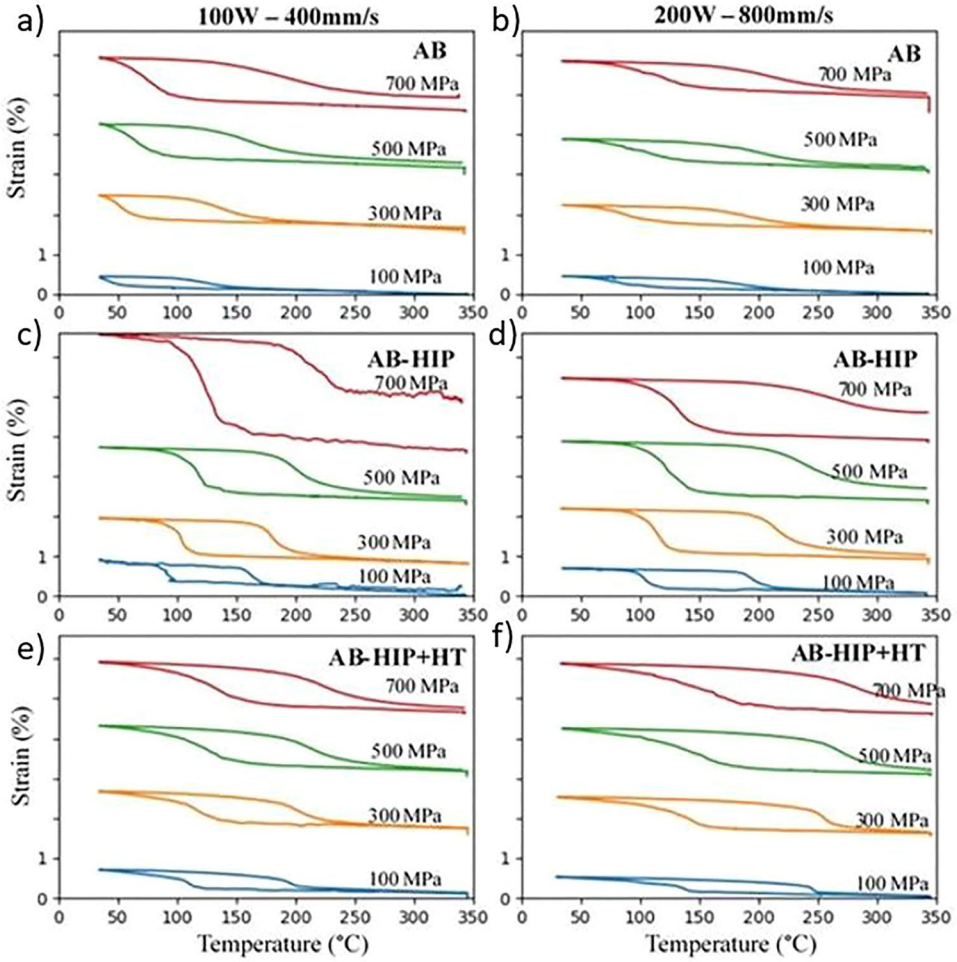

Fig. 5 Strain-Temperature curves of different conditions: (**a**) 100W-AB, (**b**) 200W-AB, (**c**) 100W-AB-HIP, (**d**) 200W-AB-HIP, (**e**) 100W-AB-HIP + HT, and (**f**) 200W-AB-HIP + HT

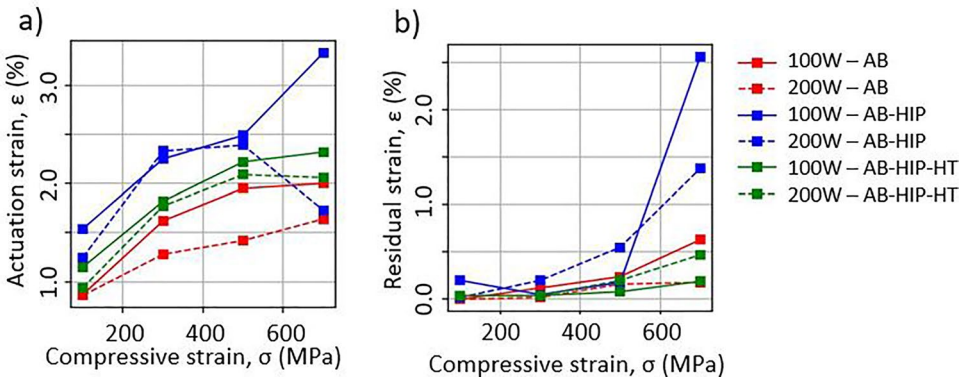

Fig. 6 Actuation strain (**a**) and residual strain (**b**) for samples fabricated with different laser powers and post-processing conditions

martensite and precipitate can be accommodated, forming a large martensite plate by absorbing the precipitate during its growth [40, 41] resulting in higher transformation strains. Thus, HIP will homogenize the material and precipitate small H-phase grains that lead to a larger actuation strain regarding AB conditions. However, the presence of the oxides will increase the residual strain. Oxides do not present shape memory behavior. The literature shows that non-transforming phases can limit the reverse transformation and induce residual strain [41]. Therefore, we suppose that the presence of oxide in the matrix can favor the residual strain.

After solution treatment and aging, the shape memory effect was significantly improved in the samples, still with lower actuation strains. Actuation strains of 1.82%, 2.23%, and 2.33% without accumulation of noticeable residual strains were achieved for the 100W-AB + HT samples at 300 MPa, 500 MPa, and 700 MPa, respectively. The same trend was seen for the 200W-AB + HT condition with lower

values for actuation strain, still, the residual strains were significantly lower than the HIP condition with the highest value of 0.47% at 700 MPa. The decrease in actuation strains compared to the HIP condition is probably due to the formation of a higher volume fraction of non-transformable precipitates after aging. Higher dimensional stability (lower residual strains) was achieved because of the formation of the precipitates and the strengthening of the matrix as a result. The existence of precipitates provides resistance to permanent deformation mechanisms such as slip in a way that twinning happens at lower stress levels before the required stress level for slip activation is achieved [40, 42]. One can note the 200W-HIP presents an outliner result at 700 MPa.

The post-treatment used in this study revealed similar small precipitates with a size of 15–20 nm in similar compositions [31]. The small size of the precipitates facilitates the propagation of the martensite twin boundaries without interruption during the transformation while providing obstacles to dislocation motion and increasing the strength as a result [31, 42, 43]. Further microstructure observations (SEM and TEM images) must be carried out to support the mechanisms mentioned in this section and give a better proportion of the role that the mechanism plays regarding the actuation and residual strain.

It should be noted that the formation of finer precipitates can also improve cyclic stability where retained martensite above the austenite finish temperatures. Also, it has been reported to be responsible for the accumulated strains after repeated cycles and precipitation can prevent this phenomenon effectively [27, 40]. Though cyclic stability is important, it was not examined in this work, and it will be left for future studies.

Conclusions

In this study, the feasibility of producing dense high-temperature shape memory alloys through laser powder bed fusion and post-treatment was assessed. Two series of parts were fabricated, maintaining the same energy density, hatch space, and layer thickness of 64 J/mm^3, 130 µm, and 30 µm, respectively. Additionally, two sets of laser power-scan speeds were utilized: 100W—400 mm/s and 200W—800 mm/s. The effect of process parameters, HIP treatment, and heat treatment on the microstructure and thermomechanical behavior of the fabricated parts were investigated. The main findings are outlined as follows:

1. Density can be improved through the change of process parameters or HIP treatment. The former method leads to compositional changes. It is noteworthy that there is no prior report of HIP treatment of $NiTiHf_{20}$ alloy. Follow-up studies are needed to determine the optimum parameters for the HIP process of this alloy.
2. Transformation temperature of as-built samples exhibit broadened peaks due to factors like composition variations, dislocations, and residual stress. Differences in transformation temperatures between samples stem from Ni content variations and inclusion formation influenced by LPBF parameters. Heat treatments alter transformation behavior, with HIP showcasing multi-stage peaks linked to Ni depletion and H-phase reinforcement. Aging creates uniformly dispersed H-phase precipitates, enhancing material strength, while Ni depletion contributes to rising transformation temperatures.
3. Impurity pick-up and Ni evaporation are the main factors that change the compositions, transformation temperatures, and thermomechanical behavior. The impurities are mainly in the form of HfO_2 and $(Ti+Hf)_4Ni_2O_x$. These non-transforming inclusions increase the residual strain and reduce the stability of the mechanical behavior.
4. In both sets of parts, those in the HIP condition exhibited high residual strains compared to the as-built conditions. This observation was attributed to the potential dislocation annihilation, and grain coarsening due to HIP process. Although precipitates form during the slow cooling of the HIP process, their size and distribution are insufficient to improve mechanical properties.
5. Subsequent heat treatments significantly enhance the properties following HIP treatment by reducing residual strain and stabilizing mechanical behavior. In addition, the material demonstrates a significant actuation strain that is interesting in actuation applications.

Declaration

Competing interests

The authors have no relevant financial or non-financial interests to disclose.

Acknowledgements The study was supported by the European Commission through the CPER DURABIMAT EU000902.

Author Contributions TC: writing, conceptualization, data curation, investigation. MN: writing, conceptualization, data curation, investigation, review and editing. KS: resources. LS-S: resources, investigation, review and editing. LP: resources. SV: investigation, review. PJ: resources. MA: resources. OB; resources. SAC: supervision, review and editing. ME: investigation, supervision.

Funding The authors declare that no funds, grants, or other support were received during the preparation of this manuscript.

Data Availability Not available.

References

1. Elahinia M et al (2018) Additive manufacturing of NiTiHf high temperature shape memory alloy. Scr Mater 145:90–94. https://doi.org/10.1016/j.scriptamat.2017.10.016
2. Karaca HE et al (2013) Effects of nanoprecipitation on the shape memory and material properties of an Ni-rich NiTiHf high temperature shape memory alloy. Acta Mater 61(19):7422–7431. https://doi.org/10.1016/j.actamat.2013.08.048
3. Van Humbeeck (2012) Shape memory alloys with high transformation temperatures. In: Materials Research Bulletin, Proceedings of the IFFM2011 (2011 International Forum on Functional Materials) and AFM-2 (2nd Special Symposium on Advances in Functional Materials) 47(10):2966–68. https://doi.org/10.1016/j.materresbull.2012.04.118.
4. Kirmacioglu KE, Kaynak Y, Benafan O (2019) Machinability of Ni-rich NiTiHf high temperature shape memory alloy. Smart Mater Struct 28(5):055008. https://doi.org/10.1088/1361-665X/ab02a2
5. Zhang M et al (2022) Tailoring the superelasticity of NiTi alloy fabricated by directed energy deposition through the variation of residual stress. Mater Dess 224:111311. https://doi.org/10.1016/j.matdes.2022.111311
6. Parvizi S et al (2021) Effective parameters on the final properties of NiTi-based alloys manufactured by powder metallurgy methods: a review. Prog Mater Sci 117:100739. https://doi.org/10.1016/j.pmatsci.2020.100739
7. Alagha AN, Hussain S, Zaki W (2021) Additive manufacturing of shape memory alloys: a review with emphasis on powder bed systems. Mater Des 204:109654. https://doi.org/10.1016/j.matdes.2021.109654
8. Saedi S et al (2016) Thermomechanical characterization of Ni-rich NiTi fabricated by selective laser melting. Smart Mater Struct 25(3):035005. https://doi.org/10.1088/0964-1726/25/3/035005
9. Saedi S et al (2018) On the effects of selective laser melting process parameters on microstructure and thermomechanical response of Ni-rich NiTi. Acta Mater 144:552–560. https://doi.org/10.1016/j.actamat.2017.10.072
10. Ren Q et al (2022) Effect of a constant laser energy density on the evolution of microstructure and mechanical properties of NiTi shape memory alloy fabricated by laser powder bed fusion. Opt Laser Technol 152:108182. https://doi.org/10.1016/j.optlastec.2022.108182
11. Khademzadeh S et al (2020) Quality enhancement of microstructure and surface topography of NiTi parts produced by laser powder bed fusion. CIRP J Manuf Sci Technol 31:575–582. https://doi.org/10.1016/j.cirpj.2020.08.009
12. Khanlari K et al (2021) Effects of printing volumetric energy densities and post-processing treatments on the microstructural properties, phase transformation temperatures and hardness of near-equiatomic NiTinol parts fabricated by a laser powder bed fusion technique. Intermetallics 131:107088. https://doi.org/10.1016/j.intermet.2021.107088
13. Guo W et al (2022) Effect of laser scanning speed on the microstructure, phase transformation and mechanical property of NiTi alloys fabricated by LPBF. Mater Des 215:110460. https://doi.org/10.1016/j.matdes.2022.110460
14. Sabahi N et al (2020) A review on additive manufacturing of shape-memory materials for biomedical applications. JOM 72(3):1229–1253. https://doi.org/10.1007/s11837-020-04013-x
15. Hou H et al (2019) Fatigue-resistant high-performance elastocaloric materials made by additive manufacturing. Science 366(6469):1116–1121. https://doi.org/10.1126/science.aax7616
16. Lauhoff C et al (2020) Additive manufacturing of Co-Ni-Ga high-temperature shape memory alloy: processability and phase transformation behavior. Metall Mater Trans A 51(3):1056–1061. https://doi.org/10.1007/s11661-019-05608-z
17. Lauhoff C et al (2020) Excellent superelasticity in a Co-Ni-Ga high-temperature shape memory alloy processed by directed energy deposition. Mater Res Lett 8:314–320. https://doi.org/10.1080/21663831.2020.1756495
18. Li W et al (2020) The combined influence of grain size distribution and dislocation density on hardness of interstitial free steel. J Mater Sci Technol 45:35–43. https://doi.org/10.1016/j.jmst.2019.11.025
19. Nematollahi M et al (2020) Laser powder bed fusion of NiTiHf high-temperature shape memory alloy: effect of process parameters on the thermomechanical behavior. Metals 10(11):1522. https://doi.org/10.3390/met10111522
20. Toker GP et al (2020) Shape memory behavior of NiTiHf alloys fabricated by selective laser melting. Scr Mater 178:361–365. https://doi.org/10.1016/j.scriptamat.2019.11.056
21. Nematollahi M et al (2019) Additive manufacturing of Ni-Rich NiTiHf20: manufacturability, composition, density, and transformation behavior. Shape Memory Superelasticity 5(1):113–124. https://doi.org/10.1007/s40830-019-00214-9
22. Dabbaghi H, Safaei K, Nematollahi M, Bayati P, Elahinia M (2020) Additively manufactured NiTi and NiTiHf alloys: estimating service life in high-temperature oxidation. Materials 13(9):2104. https://doi.org/10.3390/ma13092104
23. Karakoc O, Hayrettin C, Canadinc D, Karaman I (2018) Role of applied stress level on the actuation fatigue behavior of NiTiHf high temperature shape memory alloys. Acta Mater 153:156–168. https://doi.org/10.1016/j.actamat.2018.04.021
24. Bassini E et al (2022) Effects of the solution and first aging treatment applied to as-built and post-HIP CM247 produced via laser powder bed fusion (LPBF). J Alloy Compd 905:164213
25. Oliveira JP, Schell N, Zhou N, Wood L, Benafan O (2019) Laser welding of precipitation strengthened Ni-rich NiTiHf high temperature shape memory alloys: microstructure and mechanical properties. Mater Des 162:229–234
26. Shen J et al (2021) In-situ synchrotron X-ray diffraction analysis of the elastic behaviour of martensite and H-phase in a NiTiHf high temperature shape memory alloy fabricated by laser powder bed fusion. Addit Manuf Lett 1:100003
27. Benafan O (2012) Deformation and phase transformation processes in polycrystalline NiTi and NiTiHf high temperature shape memory alloys
28. Olier P et al (1997) Effects of impurities content (oxygen, carbon, nitrogen) on microstructure and phase transfSormation temperatures of near equiatomic TiNi shape memory alloys. J. Phy. IV 07:C5-143–C5-148. https://doi.org/10.1051/jp4:1997522.
29. Jamshidi P, Panwisawas C, Langi E, Cox SC, Feng J, Zhao L, Attallah MM (2022) Development, characterisation, and modelling of processability of nitinol stents using laser powder bed fusion. J. Alloys Compds. 909:164681. https://doi.org/10.1016/j.jallcom.2022.164681
30. Han Q et al (2018) Laser powder bed fusion of Hastelloy X: Effects of hot isostatic pressing and the hot cracking mechanism. Mater Sci Eng A 732:228–239. https://doi.org/10.1016/j.msea.2018.07.008

31. Benafan O et al (2021) Processing and scalability of NiTiHf high-temperature shape memory alloys. Shape Memory Superelasticity 7(1):109–165. https://doi.org/10.1007/s40830-020-00306-x
32. Marattukalam JJ et al (2018) Effect of heat treatment on microstructure, corrosion, and shape memory characteristics of laser deposited NiTi alloy. J Alloy Compd 744:337–346. https://doi.org/10.1016/j.jallcom.2018.01.174
33. Xue L et al (2021) Controlling martensitic transformation characteristics in defect-free NiTi shape memory alloys fabricated using laser powder bed fusion and a process optimization framework. Acta Mater 215:117017. https://doi.org/10.1016/j.actamat.2021.117017
34. Karbakhsh Ravari B, Farjami S, Nishida M (2014) Effects of Ni concentration and aging conditions on multistage martensitic transformation in aged Ni-rich TiNi alloys. Acta Mater 69:17–29. https://doi.org/10.1016/j.actamat.2014.01.028
35. Yang F, Coughlin DR, Phillips PJ, Yang L, Devaraj A, Kovarik L, Noebe RD, Mills MJ (2013) Structure analysis of a precipitate phase in an Ni-rich high-temperature nitihf shape memory alloy. Acta Mater 61(9):3335–3346. https://doi.org/10.1016/j.actamat.2013.02.023
36. Meng XL et al (2006) Effect of aging on martensitic transformation and microstructure in Ni-rich TiNiHf shape memory alloy. Scr Mater 54:1599–1604. https://doi.org/10.1016/j.scriptamat.2006.01.017
37. Sadrnezhaad SK, Mashhadi F, Sharghi R (1997) Heat treatment of Ni-Ti alloy for improvement of shape memory effect. Mater Manuf Process 12:107–115. https://doi.org/10.1080/10426919708935124
38. Sehitoglu H, Wu Y, Patriarca L, Li G, Ojha A, Zhang S, Chumlyakov Y, Nishida M (2017) Superelasticity and shape memory behavior of NiTiHf alloys. Shape Memory Superelasticity 3(2):168–187. https://doi.org/10.1007/s40830-017-0108-1
39. Kockar B et al (2006) A method to enhance cyclic reversibility of NiTiHf high temperature shape memory alloys. Scr Mater 54(12):2203–2208. https://doi.org/10.1016/j.scriptamat.2006.02.029
40. Saghaian SM et al (2016) Tensile shape memory behavior of Ni50.3Ti29.7Hf20 high temperature shape memory alloys. Mater Des 101:340–345. https://doi.org/10.1016/j.matdes.2016.03.163
41. Frenzel J, George EP, Dlouhy A, Somsen Ch, Wagner MF-X, Eggeler G (2010) Influence of Ni on martensitic phase transformations in NiTi shape memory alloys. Acta Mater 58(9):3444–3458. https://doi.org/10.1016/j.actamat.2010.02.019
42. Santamarta R et al (2013) TEM study of structural and microstructural characteristics of a precipitate phase in Ni-rich NiTiHf and NiTiZr shape memory alloys. Acta Mater 61(16):6191–6206. https://doi.org/10.1016/j.actamat.2013.06.057
43. Bigelow GS et al (2011) Load-biased shape-memory and superelastic properties of a precipitation strengthened high-temperature Ni50.3Ti29.7Hf20 alloy. Scripta Mater 64(8):725–728. https://doi.org/10.1016/j.scriptamat.2010.12.028